LETTER

doi:10.1038/nature22042

Continental crust formation on early Earth controlled by intrusive magmatism

A. B. Rozel[1], G. J. Golabek[2], C. Jain[1], P. J. Tackley[1] & T. Gerya[1]

The global geodynamic regime of early Earth, which operated before the onset of plate tectonics, remains contentious. As geological and geochemical data suggest hotter Archean mantle temperature[1,2] and more intense juvenile magmatism than in the present-day Earth[3,4], two crust–mantle interaction modes differing in melt eruption efficiency have been proposed: the Io-like heat-pipe tectonics regime dominated by volcanism[5,6] and the "Plutonic squishy lid" tectonics regime governed by intrusive magmatism, which is thought to apply to the dynamics of Venus[7–9]. Both tectonics regimes are capable of producing primordial tonalite–trondhjemite–granodiorite (TTG) continental crust[5,10] but lithospheric geotherms and crust production rates as well as proportions of various TTG compositions differ greatly[9,10], which implies that the heat-pipe and Plutonic squishy lid hypotheses can be tested using natural data[11]. Here we investigate the creation of primordial TTG-like continental crust using self-consistent numerical models of global thermochemical convection associated with magmatic processes. We show that the volcanism-dominated heat-pipe tectonics model results in cold crustal geotherms and is not able to produce Earth-like primordial continental crust. In contrast, the Plutonic squishy lid tectonics regime dominated by intrusive magmatism results in hotter crustal geotherms and is capable of reproducing the observed proportions of various TTG rocks. Using a systematic parameter study, we show that the typical modern eruption efficiency of less than 40 per cent[12] leads to the production of the expected amounts of the three main primordial crustal compositions previously reported from field data[4,11] (low-, medium- and high-pressure TTG). Our study thus suggests that the pre-plate-tectonics Archean Earth operated globally in the Plutonic squishy lid regime rather than in an Io-like heat-pipe regime.

To understand the global geodynamic regime of the Archean pre-plate-tectonics Earth an analytical explanation comparable to that of modern plate tectonics is needed, which can be validated and elaborated on using a continually expanding set of observational and analytical data[13,14]. The lack of consensus and ongoing controversy is attributable to the scarcity and fundamental unavailability of data[14]. Therefore, numerical modelling has an increasingly important role in developing and testing geodynamic hypotheses based on robust observations aimed at explaining the evolution of the pre-plate-tectonics Archean Earth[5,6,9,10,15].

Geological and geochemical data suggest an Archean mantle hotter than today's[1,2] and intense juvenile magmatism[3,4], but the exact nature of these tectono-magmatic crust–mantle interactions remains debatable. Using thermochemical mantle convection models, Moore and Webb[5] suggested an Io-like heat-pipe tectonic regime as a framework for Archean geodynamics. Dominated by volcanism (100% eruption efficiency), the heat is transported to the surface by mantle-derived melt rising through narrow conduits. It has been demonstrated that the heat-pipe model produces a cold thickened crust followed by delamination from the bottom of the crust into the hot convecting Archean mantle in the form of partially molten eclogitic drips, which could be responsible for the formation of primordial TTG-like continental crust[5,6,9,10]. The fully volcanic production of crust modelled in ref. 5 can generate various temperature profiles in the lithosphere. However, the eruption rate was not obtained self-consistently in their study and geological field data[12] suggest a predominantly intrusive magmatism. We show here that a fully eruptive magmatism generates a lithosphere that is too cold to form TTGs (and hence a plausible geodynamics model), which could explain why the heat-pipe model is not universally accepted and uniformitarian Eoarchean plate tectonic models are still debated[7,16].

An alternative tectonic regime—the Plutonic squishy lid—for Archean Earth involves predominantly intrusive mantle-derived magmatism[7–9], resulting in a hot, thickened crust subjected to internal overturns[17] and episodic recycling into the mantle[9,10]. The efficient mantle heat release in this geodynamic mode is assisted by magmatism-induced crustal convection and strongly enhanced geothermal gradients in the thinned brittle upper crust[9,10]. Primordial TTG-like melts form at both crustal and mantle depths by a variety of processes including (1) delamination and dripping of the lower mafic crust into the mantle; (2) local thickening of the crust; and (3) small-scale crustal overturns[10].

Present-day geological observations show that a large fraction of mantle-derived melt is intruded at depth with ratios of intrusive versus extrusive melt volumes ranging between 4:1 and 10:1 (melt eruption efficiency 9%–20%) in large-scale magmatic settings[12]. However, it remains uncertain whether these observations can be extrapolated to the Archean eon. In numerical models, the eruption and intrusion efficiencies must be assumed and treated as separate processes. A partially molten region in the asthenosphere would just stagnate below the lithosphere if no additional magma transport were to be implemented. Numerical models assuming instantaneous magma transport from asthenosphere to crust suggest that the assumed eruption efficiency notably affects the pressure–temperature conditions of TTG-melt formation and hence the proportions of various primordial continental crust compositions[9,10].

Field studies have shown that TTGs can make up between half and two-thirds of the Archean crust and can be classified into three different types (low-, medium- and high-pressure TTGs), each having a specific pressure–temperature window of formation[11]. Moyen[11] has estimated the present-day volumes of low-, medium- and high-pressure TTGs to be 20%, 60% and 20%, respectively. This creates an opportunity to test the two proposed Archean geodynamic regimes on the basis of natural data. Unlike previous relatively short-term regional-scale models[5,6,9,10], such a test should employ long-term global-scale self-consistent numerical models of thermochemical mantle convection associated with magmatic processes leading to crustal growth and recycling.

Here, we use the latest version of a global two-dimensional mantle convection model[18] (see Methods) to study the evolution of the Archean Earth between 4 and 3 billion years ago. We track whether the specific conditions for the formation of each TTG type have been met and

[1]Institute of Geophysics, ETH Zurich, 8092 Zurich, Switzerland. [2]Bayerisches Geoinstitut, University of Bayreuth, 95440 Bayreuth, Germany.

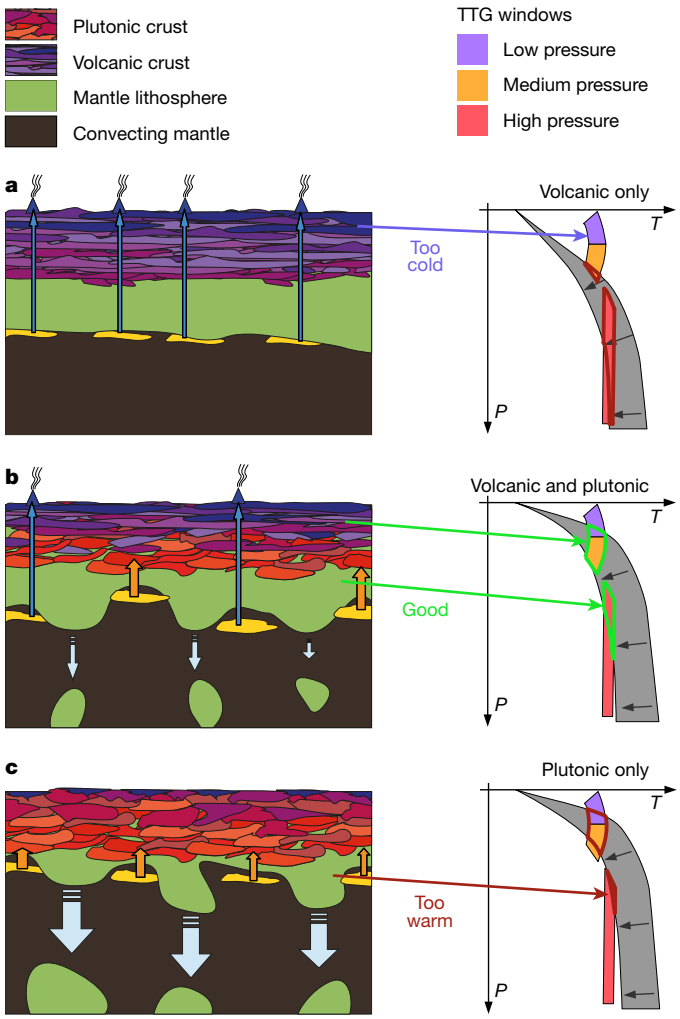

Figure 1 | The impact of the emplacement mechanism on the geotherm. **a**, 100% eruption efficiency; **b**, mix of eruption and intrusion; and **c**, intrusive emplacement only. The grey envelopes in the right-hand-side plots show the temporal evolution of the geotherm. The pressure–temperature windows in which TTG can be created[11] are also represented.

integrate their volumes over time for a billion years (see the pressure–temperature coloured windows in the right plots of Fig. 1, Extended Data Table 1 and Methods for details). We systematically test the influence of the volumetric melt eruption efficiency on the convection regimes and on the volumes and relative proportions of TTGs that are generated. An eruption efficiency is imposed in each simulation and the convection regimes obtained are always fully self-consistent. Figure 1 represents the different emplacement scenarios and their impact on the intersection of geotherms, with the pressure–temperature windows for TTG creation. In our models, the eruption efficiency represents the volumetric percentage of mantle-derived melt that is erupted to the surface and forms volcanic crust (blue arrows in Fig. 1). Its temperature is instantaneously set to surface temperature (300 K). The remaining melt is intruded at the bottom of the crust (that is, at the Mohorovičić discontinuity; orange arrows in Fig. 1) and retains the high temperature of the melt source in the mantle. Low eruption efficiency (below 30%) implies a large intrusion percentage and generates a very warm crust and weak lithosphere (Fig. 1c). In contrast, high eruption efficiency (above 70%) results in reduced intrusion efficiency and, therefore, reduced heating of the crust (Fig. 1a). This generates a cold crust and a strong lithosphere[5,18].

In addition to the eruption efficiency, we systematically varied the internal friction coefficient of the lithosphere, which strongly influences both global and regional lithospheric dynamics[8,19]. We test values of the friction coefficient f within the experimentally measured range[20] from 0.1 to 0.6.

Figure 2 depicts the time dependence of various fields in the reference simulation (friction coefficient 0.2, eruption efficiency 30%, corresponding to Fig. 1b), leading to Earth-like primordial crust formation. We documented three main types of tectonic mode in the reference simulation (Fig. 2d): dripping, resurfacing and stagnant lid. The dripping mode (Fig. 2a, left plot) is characterized by blocks of basaltic crust (of various sizes, depending on the stage) detaching from the bottom of the lithosphere. A Venus-like[21,22] resurfacing episode (Fig. 2a, right plot) is characterized by a very large part of the lithosphere or even the entire lithosphere (as observed in this specific case) suddenly sinking into the mantle. The stagnant lid mode (Fig. 2a, centre plot) is characterized by no substantial deformation in the lithosphere. The stagnant lid mode can be observed during early stages when basalt accumulates at the core–mantle boundary owing to intense eclogitic dripping from the lithosphere. This cold and viscous basal eclogitic layer temporarily insulates the core, suppressing plumes for tens and sometimes hundreds of millions of years. The stagnant lid mode can also be reached during later stages when the mantle depletion prevents the further generation of basalt and thus future dripping events (see Fig. 2d).

Figure 2b–d shows how each type of TTG rock is produced at different stages. Low-pressure TTGs are predominantly generated when the lithosphere is very thin and warm. This occurs either early on while the mantle is still very warm or during a global resurfacing event. Medium-pressure TTGs are produced during the dripping phases, both during early and later stages or after a major resurfacing when the lithosphere thickens. Stagnant lid episodes tend to shut down the generation of medium-pressure TTGs because of the progressive thickening and cooling of the lithosphere. Finally, formation of high-pressure TTGs occurs when both the lithosphere and the basaltic crust are sufficiently thick and cold. During the last 300 million years of the simulation no new high-pressure TTGs are formed, because the crust present after the resurfacing event is insufficiently thick. Figure 1 also shows the time evolution of the geotherm (black arrows). The temperature profiles of the lithosphere cross the pressure–temperature conditions for TTG creation at different times.

Figure 3a and Extended Data Table 2 show the expected total volumes of TTG rocks created by the end of the simulations. The numerical results clearly demonstrate that the eruption efficiency has to be rather low (around 20%–40%) and thus similar to modern values[12] to both generate a substantial volume of TTG rocks within a billion years (about 1.5×10^9 km^3) and reproduce the expected proportions of each TTG type (Fig. 3b and c). In contrast, the 100% eruption efficiency proposed in ref. 5 produces a hundred times less of the low- and medium-pressure TTGs, resulting in a thin and predominantly high-pressure primordial TTG crust (with a volume of 8×10^8 km^3). We can thus conclude that whereas high-pressure TTGs can be produced for any intrusion fraction, medium- and low-pressure TTGs require that a majority of the mantle-derived melt intrudes into the crust instead of being erupted at the surface.

Additionally, we systematically investigated the influence of the lithospheric friction coefficient on the TTG crust production. Our simulations show that a reduced friction coefficient of 0.2 allows for optimal TTG formation conditions. The simulations using a higher friction coefficient of 0.3–0.6 are less favourable and overestimate the relative amount of high-pressure TTGs owing to increased thickness and decreased temperature of the lithosphere and crust. On the other hand, the simulation with very weak lithosphere (friction coefficient 0.1) fails to generate a substantial amount of high-pressure TTGs because the lithosphere remains too thin and warm during the entire simulation.

The realistic proportions of TTGs obtained in simulations using a friction coefficient of 0.2 and high intrusion fraction is due to a simultaneous increase of low-pressure TTG production and decrease

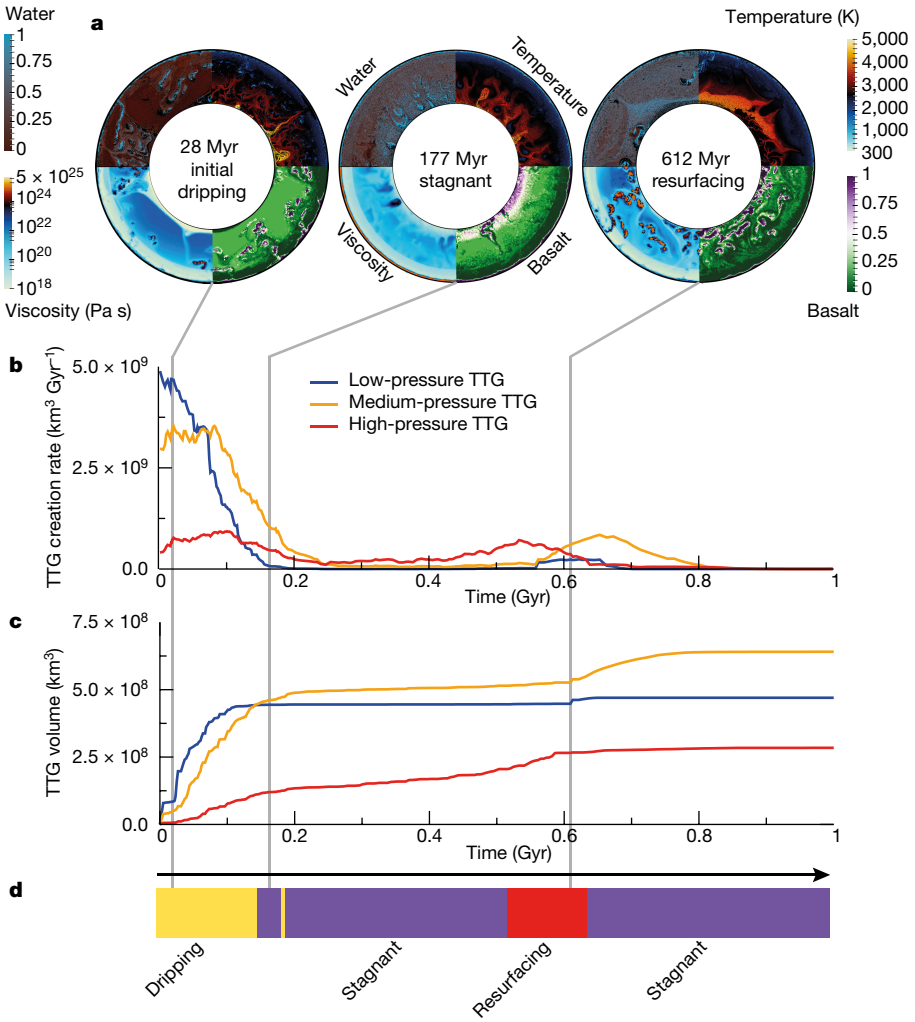

Figure 2 | Time evolution of the reference model. This case was performed with a friction coefficient of 0.2 and an intrusion fraction of 0.7. **a**, Two-dimensional fields for three selected times. **b**, TTG creation rate. **c**, Cumulative volume of each type of TTG. **d**, Convection regimes self-consistently obtained throughout time. Source Data accompanies this figure online.

of high-pressure TTG production, bringing their ratio to around 1:1 (Fig. 3b and c), similar to the observed natural data[11]. A sufficiently low friction coefficient (0.2) thus ensures the regular (but not too frequent) formation of mechanical instabilities (drips) in the lithosphere, thinning the lithosphere enough to decrease the volume of high-pressure TTGs and increase the volume of low-pressure TTGs.

Figure 2b shows that our average global TTG crustal growth rates from the reference model are strikingly consistent with Archean continental crustal growth rates estimated from natural data (0.8–3.0 km^3 per year[4]). We show that TTG production rates of up to 10 km^3 per year can occur as a result of very vigorous initial dripping. Moreover, all types of TTG can also be created during global resurfacing events or what would be the onset of plate tectonics. Figure 2b and c shows that low-pressure TTG can be produced during a resurfacing event, but most of the volume in our case comes from the initial dripping stage. A substantial portion of medium-pressure TTG can be expected to appear during tectonic events at any point in the evolution of Earth. The high-pressure TTG rocks seem to form during any convection regime, but cannot be created after a major resurfacing event because a sufficiently thick basaltic crust cannot be quickly established. Therefore, our numerical models show that low-pressure TTGs on Earth should have been predominantly produced during the earliest dripping stages, high-pressure TTGs could have been produced at any age before a major overturn (or the onset of plate tectonics), while medium-pressure TTGs can be produced at any time.

In Extended Data Table 2, we report the final volumes of TTG produced after one billion years. Using field data, Dhuime *et al.*[4] report that 3×10^9 km^3 of continental crust has been produced after one billion years. Moyen[11] estimated that TTG rocks represent half of the total volume of continental crust (also composed of other magmatic and sedimentary rocks). Extended Data Table 2 shows that our models produce up to 1.5×10^9 km^3, which is exactly the expected volume of TTG rocks (that is, half the volume of continental crust proposed by Dhuime *et al.*[4]). This volume is obtained in several cases with an intrusion efficiency of 50% and higher. Our simulations are thus not only able to generate the appropriate relative proportions of TTG rocks but can also produce the expected total amount of these rocks on a global scale.

Our numerical models thus suggest that a combination of low eruption efficiency (20%–40%) with reduced brittle/plastic strength of the lithosphere (friction coefficient about 0.2) is necessary to reproduce the observed distribution and volumes of TTG rocks. This implies that the eruption efficiency in the Archean was similar to present-day values[12], whereas the brittle/plastic strength of the lithosphere was reduced compared to dry conditions[20], presumably owing to the widespread magmatic weakening of the lithosphere by mantle-derived melts[10,14]. We therefore suggest that the early Archean Earth operated globally in the Plutonic squishy lid tectonics mode[7–9], implying a low eruption efficiency and relatively warm lithosphere subjected to dripping and global resurfacing processes. In contrast, an Io-like heat-pipe tectonic mode[5,6] assuming 100% eruption efficiency and relatively

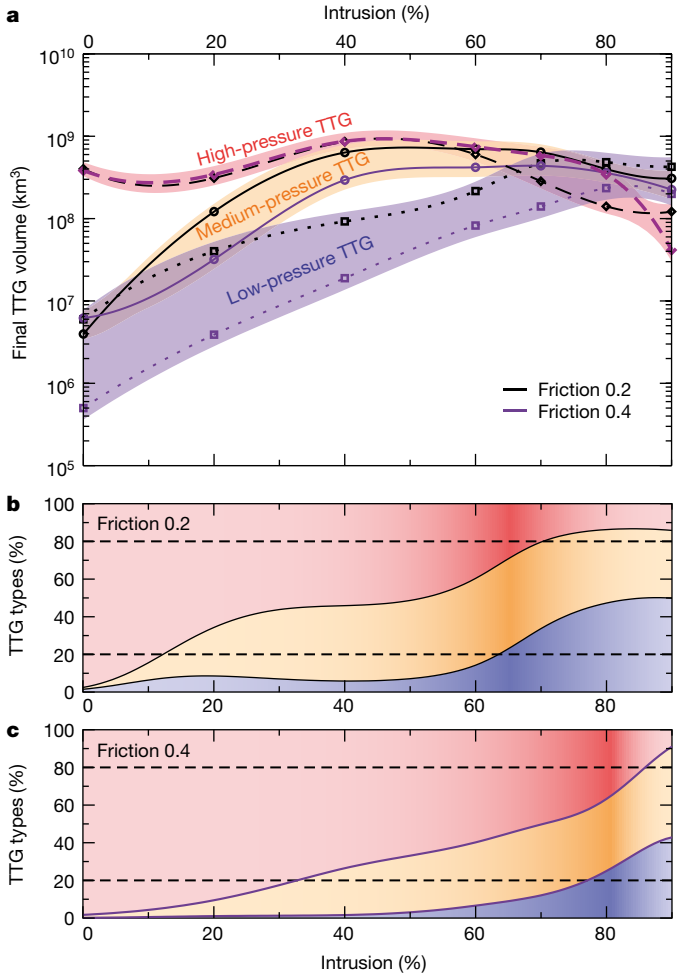

Figure 3 | Amount of all TTG types produced in our models. a, Volumes of each type of TTG produced over a billion years. For clarity, only two friction coefficients are shown (0.2 and 0.4). **b**, **c**, The solid curves show the relative percentages of TTG types produced as a function of the intrusion efficiency. The dashed lines show the expected values from ref. 11. The two cases (friction coefficients 0.2 and 0.4) presented in **a** are shown. The darker areas show where simulations best match data. Source Data accompanies this figure online.

cold lithosphere seems unlikely because it results in predominantly high-pressure TTG crust inconsistent with the natural record.

Online Content Methods, along with any additional Extended Data display items and Source Data, are available in the online version of the paper; references unique to these sections appear only in the online paper.

Received 28 September 2016; accepted 21 February 2017.
Published online 8 May 2017.

1. Herzberg, C. & Gazel, E. Petrological evidence for secular cooling in mantle plumes. *Nature* **458,** 619–622 (2009).
2. Condie, K., Aster, R. & van Hunen, J. A great thermal divergence in the mantle beginning 2.5 Ga: geochemical constraints from greenstone basalts and komatiites. *Geosci. Frontiers* **7,** 543–553 (2016).
3. Condie, K. Accretionary orogens in space and time. *Geol. Soc. Am.* **200,** 145–158 (2007).
4. Dhuime, B., Hawkesworth, C., Cawood, P. & Storey, C. A change in the geodynamics of continental growth 3 billion years ago. *Science* **335,** 1334–1336 (2012).
5. Moore, W. & Webb, A. Heat-pipe earth. *Nature* **501,** 501–505 (2013).
6. Johnson, T., Brown, M., Kaus, B. & VanTongeren, J. Delamination and recycling of Archaean crust caused by gravitational instabilities. *Nat. Geosci.* **7,** 47–52 (2014).
7. Van Kranendonk, M. Two types of Archean continental crust: plume and plate tectonics on early earth. *Am. J. Sci.* **310,** 1187–1209 (2010).
8. Gerya, T., Stern, R., Baes, M., Sobolev, S. & Whattam, S. Plate tectonics on the Earth triggered by plume-induced subduction initiation. *Nature* **527,** 221–225 (2015).
9. Fischer, R. & Gerya, T. Early earth plume-lid tectonics: a high-resolution 3d numerical modelling approach. *J. Geodyn.* **100,** 198–214 (2016).
10. Sizova, E., Gerya, T., Stüwe, K. & Brown, M. Generation of felsic crust in the Archean: a geodynamic modeling perspective. *Precambr. Res.* **271,** 198–224 (2015).
11. Moyen, J. The composite Archaean grey gneisses: petrological significance, and evidence for a non-unique tectonic setting for Archaean crustal growth. *Lithos* **123,** 21–36 (2011).
12. Crisp, J. A. Rates of magma emplacement and volcanic output. *J. Volcanol. Geotherm. Res.* **20,** 177–211 (1984).
13. Benn, K., Mareschal, J.-C. & Condie, K. in *Archean Geodynamics and Environments* (eds Benn, K., Mareschal, J.-C. & Condie, K.) 1–5 (AGU, 2006).
14. Gerya, T. Precambrian geodynamics: concepts and models. *Gondwana Res.* **25,** 442–463 (2014).
15. Rey, P., Coltice, N. & Flament, N. Spreading continents kick-started plate tectonics. *Nature* **513,** 405–408 (2014).
16. Bédard, J. A catalytic delamination-driven model for coupled genesis of Archaean crust and sub-continental lithospheric mantle. *Geochim. Cosmochim. Acta* **70,** 1188–1214 (2006).
17. de Smet, J., van den Berg, A. & Vlaar, N. The evolution of continental roots in numerical thermo-chemical mantle convection models including differentiation by partial melting. *Lithos* **48,** 153–170 (1999).
18. Lourenço, D., Rozel, A. & Tackley, P. Melting-induced crustal production helps plate tectonics on earth-like planets. *Earth Planet. Sci. Lett.* **439,** 18–28 (2016).
19. Tackley, P. J. Self consistent generation of tectonic plates in time-dependent, three dimensional mantle convection simulations. Part 1: pseudoplastic yielding. *Geochem. Geosyst. Geophys.* **1,** 1026 (2000).
20. Byerlee, J. Friction of rocks. *Pure Appl. Geophys.* **116,** 615–626 (1978).
21. Strom, R., Schaber, G. & Dawson, D. The global resurfacing of Venus. *J. Geophys. Res.* **99,** 10899–10926 (1994).
22. Armann, M. & Tackley, P. Simulating the thermochemical magmatic and tectonic evolution of Venus's mantle and lithosphere: two-dimensional models. *J. Geophys. Res.* **117,** E12003 (2012).

Acknowledgements We thank K. Condie, L. Moresi and M. Van Kranendonk for comments and suggestions as part of the review process. A.B.R. and C.J. received funding from the European Research Council under the European Union's Seventh Framework Programme (FP/20072013)/ERC Grant Agreement number 320639 project iGEO. T.G. received support from the SNF projects Swiss-AlpArray and number 200020_166063.

Author Contributions A.B.R., G.J.G., C.J. and T.G. designed the set of numerical simulations. P.J.T. implemented the eruption–intrusion routines in the convection code. A.B.R. wrote all postprocessing routines and produced the figures. All authors contributed to the manuscript.

Author Information Reprints and permissions information is available at www.nature.com/reprints. The authors declare no competing financial interests. Readers are welcome to comment on the online version of the paper. Publisher's note: Springer Nature remains neutral with regard to jurisdictional claims in published maps and institutional affiliations. Correspondence and requests for materials should be addressed to A.B.R. (antoine.rozel@erdw.ethz.ch).

Reviewer Information *Nature* thanks K. Condie, L. Moresi and M. Van Kranendonk for their contribution to the peer review of this work.

METHODS

Numerical modelling of thermochemical convection. Thermochemical compressible convection is studied using the code StagYY[23] in two-dimensional spherical annulus geometry[24]. Equations of momentum, mass and energy conservation are solved using a parallel MUMPS solver available in the PETSc package[25]. The finite difference approximation is used on a staggered grid[26] with a radially varying resolution (higher in the boundary layers and at the 660 phase transition). The domain is discretized by 64 (radial) times 512 (lateral) cells. Free slip boundary conditions are used for both outer and inner boundaries. The surface temperature is fixed at 300 K and the initial core temperature is at 6,000 K.

A tracer field is advected through the mesh using second-order divergence-free spatial interpolation of the velocity field and a fourth-order Runge–Kutta scheme through time. Each tracer carries several quantities, such as water content, composition, temperature and radiogenic heating rate. Using these fields on tracers limits numerical diffusion. Radiogenic elements are partitioned during melting: basaltic melts are 100 times more enriched than their solid residue. For simplicity water is considered to penetrate fully into the top 10 km and is advected throughout the mantle. The compositional model treats solid and molten rocks as being a linear combination of basalt (crustal material) and harzburgite (depleted mantle). The primordial mantle starts with an initial petrological composition of 20% basalt and 80% harzburgite, being a mixture of 60% olivine and 40% pyroxene-garnet. For numerical efficiency the composition is stored on tracers, while the melting calculations are performed on the mesh. For this purpose a meshed composition field is computed at cell centres by averaging the tracers within the cell. On the mesh, a melt fraction is computed at every time step, comparing the pressure–temperature conditions to a composition-dependent solidus function, considering a latent heat of 600 kJ kg^{-1}. Once the amount of melt is computed on the mesh, the corresponding mass of molten material is created on the tracer field. If melting occurs at less than 300 km depth, molten tracers of fully basaltic composition are transported either to the top of the domain (eruption) or to the bottom of the crust (intrusion). The temperature of the erupted tracers is set to surface temperature, rapidly forming a cold lithosphere. The temperature of intruded tracers takes only adiabatic decompression into account, resulting in a warm lithosphere. The column of material between the melt source region and the intrusion or eruption location is instantaneously advected downwards to conserve mass. The solid residue left behind by the eruption–intrusion procedure is pure harzburgite. For more details regarding the implementation see refs 27 and 28. The viscosity is both depth- and temperature-dependent following the Arrhenius formulation (see ref. 18 for details). The density is computed as the sum of pressure, thermal and compositional effects, including solid–solid phase transitions. Olivine and pyroxene-garnet phases are treated separately, so the density increase associated with the basalt–eclogite phase transition can be taken into account. The eclogitization drives the dripping process observed during the first few hundred million years after the crystallization of the magma ocean (see ref. 18 for details).

We assume that viscous deformation operates through the diffusion creep process, which follows a temperature- and pressure-dependent Arrhenius law:

$$\eta_{\mathrm{diff}}(T,P)=\eta_0\Delta\eta_i\exp\left(\frac{E_i+PV_i}{RT}-\frac{E_i}{RT_0}\right) \quad (1)$$

where η_0 is the reference viscosity (10^{20} Pa s) at zero pressure and reference temperature T_0 (1,600 K), $\Delta\eta$ is a factor used to impose viscosity jumps between the various layers i (up to 5 or 6), E_i is the activation energy in layer i, P is the pressure, V_i is the activation volume, R is the gas constant (8.314 J mol^{-1} K^{-1}) and T is the absolute temperature. Various values for E_i and V_i are used for the upper and lower mantle and for the post-perovskite layer close to the core–mantle boundary[29–31] (see Extended Data Table 3). In the lower mantle, the activation volume decreases with increasing pressure according to:

$$V(P)=V_i\exp\left(-\frac{P}{P_i}\right) \quad (2)$$

P_i is given in Extended Data Table 3 (or is infinity if not given). A viscosity jump of 30 is imposed at the transition between the upper and lower mantle[32].

Plastic yielding in the lithosphere is computed using a yield stress τ_y following the Byerlee approach[20]:

$$\tau_y=fP \quad (3)$$

where f is the friction coefficient. The effective viscosity is computed as:

$$\eta_{\mathrm{eff}}=\min\left(\eta_{\mathrm{diff}},\frac{\tau_y}{2\dot{\varepsilon}}\right) \quad (4)$$

where $\dot{\varepsilon}$ is the second invariant of the strain-rate tensor. The viscosity does not depend on melt fraction or composition.

Since we solve for compressible convection, the adiabatic temperature, density, thermal conductivity, thermal expansivity and heat capacity are pressure-dependent following a third-order Birch–Murnaghan equation of state, which relates the bulk modulus to pressure (see ref. 31 for a detailed explanation). Most importantly for the present study, mantle materials are treated as a mixture of olivine, pyroxene-garnet and melt phase systems, following a parameterization based on mineral physics data[33,34]. Each phase system has its own phase-transition depths and physical properties. The melt density smoothly increases with pressure. Solid olivine and pyroxene-garnet densities smoothly increase with depth too but also contain jumps at phase transitions, as shown in Extended Data Table 4. In particular, the basalt–eclogite phase transition located at a depth of around 60 km has a first-order effect on the dynamics of the lithosphere[18]. Above the eclogite phase transition, basalt is lighter than olivine by 160 kg m^{-3}. Below the phase transition, eclogite formed from basalt becomes denser than olivine by 190 kg m^{-3}, which easily drives mechanical instabilities inside the lithosphere. In the deeper mantle, both pyroxene-garnet and olivine also display density increases with depth at the boundaries of the transition zone and on top of the post-perovskite layer (see Extended Data Table 4). The pressure P_{PT} at which phase transition occurs is temperature-dependent: $P_{\mathrm{PT}}=P_0+\gamma T$, where P_0 is a reference pressure. The Clapeyron slopes γ of each transition (see Extended Data Table 4) quantify this effect.

Estimation of the volumes of TTG produced. The volumes of TTG rocks presented in Fig. 2c are obtained via a two-step process. We first compute the volume of hydrated basalt that matches the pressure–temperature conditions for TTG generation (see Extended Data Table 1 and ref. 11). To obtain what would be the volume of TTG rocks in three-dimensional spherical geometry, we compute the average global thickness produced and multiply it by the surface of the Earth for each time step t. Then we sum over all cells i of the computational domain for a certain time t and obtain an instantaneous volume of TTG:

$$v(t)=S\sum_i\frac{1}{2}\delta z_i\,C_i^{\mathrm{H_2O}}\,C_i^{\mathrm{B}} \quad (5)$$

where S is the surface of the Earth, δz_i is the thickness the cell i would have if it were spread out across the entire surface of the computational domain. $C_i^{\mathrm{H_2O}}$ is a dimensionless water concentration (1 for fully hydrated rock) and C_i^{B} is a dimensionless 'basalt concentration' (1 for basalt, 0 for harzburgite). The volume is divided by 2 under the assumption that the average degree of partial melting of hydrated basaltic crust producing TTG-melt corresponds to 50%[35]. The cell summation is performed only for cells having both water and basalt concentrations higher than half the imposed surface water content (that is, containing a large amount of hydrated basaltic crust).

The cumulative volume $V(t)$ shown in Fig. 2c is obtained by weighted time integration of the instantaneous volume $v(t)$:

$$V(t)=\int_{t'=0}^{t}\frac{v(t')}{V_{\mathrm{TTG-}P}}\frac{\partial V_{\mathrm{hbs}}}{\partial t'}\mathrm{d}t' \quad (6)$$

where $V_{\mathrm{TTG-}P}$ is the volume of rocks at pressure conditions relevant for TTG formation (a constant value) and V_{hbs} is the volume of hydrated basalt in the whole domain. We neglect rare situations in which $\partial V_{\mathrm{hbs}}/\partial t$ is negative. Equation (6) ensures that TTG is produced only when conditions relevant for their formation are matched (v is non-zero) and also when new hydrated basalt is actually formed ($\partial V_{\mathrm{hbs}}/\partial t$ is positive). This strategy is much more robust than simply integrating the volume of rock at conditions for TTG formation without any weighting. An equilibrium convection situation in which no more basalt is formed but the geotherm in the crust corresponds to TTG formation conditions would dramatically overestimate the volume of TTGs actually produced.

However, quantitative data extraction from our numerical simulations has to be considered with caution. Our simplified TTG-crust volume computation algorithm (Methods) uses an average degree of hydrated basaltic crust melting and does not directly create and trace TTG-rock regions within the crust. Regional models with direct tracing of TTG rock generally demonstrate higher crustal growth rates[10] but such tracing is not yet feasible on a global scale owing to the lack of numerical resolution. Moreover, our simplified model may overestimate the duration of stagnant lid episodes (nearly 50% of the simulation time, Fig. 2), which produce negligible amounts of TTG rock. In higher-resolution regional models the duration of such episodes is limited to about 80 million years[9,10] owing to the localized weakening of the lithosphere by magmatic processes, which is not implemented in our simplified global model. Below, we discuss the potential implications of the present study for the dynamics of Venus.

Code availability. The convection code StagYY is the property of P.J.T. and Eidgenössische Technische Hochschule (ETH) Zürich. It is available on request from P.J.T. (paul.tackley@erdw.ethz.ch).

Comparison of our numerical simulations with field observations. Comparing our numerical results with the variety and complexity of field data from Archean cratons is ambitious. While we can evaluate whether certain rheological conditions and magmatic behaviours can lead to the formation of felsic rocks on early Earth, we certainly cannot explain the complexity of petrological and geochemical data reported in the last decades. We will therefore focus on the first-order picture agreed upon in the Archean field geology community. We are confident that our numerical models give a robust answer regarding the necessary high intrusion efficiency to produce a reasonable distribution of TTG rocks. Yet, we should also keep in mind that our models are still lacking important processes, which would make a detailed comparison with field data hazardous and probably misleading, although the simple message of this study would still be valid.

First, our rheology is not composition-dependent, preventing us from producing a very stiff sub-continental lithospheric mantle. However, our viscosity is strongly temperature-dependent (as suggested by experimental data), which in itself generates a very viscous sub-crustal lithosphere. This non-trivial functionality is only possible because we use very robust parallel direct solvers[18,25]. Second, since we are looking at one billion years of global mantle evolution, the resolution in our models cannot be high enough to study the details of crustal processes, which are very valuable to field geologists who use the top-down approach (linking 'surface' data to suggest a global geodynamic picture). This important limitation does not allow us to model regional crustal processes (such as dome and keel structures) that would modify the temperature profile in the crust. Such simulations have been performed using high-resolution three-dimensional simulations[9], and suggest a picture similar to ours, but on a regional scale. Moreover, our approach is certainly valid since crustal overturn will only occur if the crust is actually produced in the first place, which we have the ability to model. Third, our petrological model is relatively simple because we want to determine which global geodynamics environment will lead to favourable conditions for TTG formation. Finally, our simulations were performed in two dimensions, because three-dimensional simulations are computationally very expensive and would not have allowed us to systematically study our parameter space. With these modelling-inherent limitations in mind, we compare features observed in our numerical models to geodynamical scenarios based on field data.

Although very few Archean rocks have been preserved on Earth, it seems widely accepted that the tectonic mode greatly changed shortly after the beginning of the Palaeoarchean, at around 3.55 billion years ago[36]. Indeed, all material older than this age (in the Eoarchean) can be found in stacked high-grade gneiss terranes, whereas felsic rocks produced later (during most of the Palaeoarchean) seem to have arisen from a less catastrophic tectonic evironment, stable enough to generate crustal diapirism[16]. There is at present no consensus on the geodynamical/tectonic process forming the various structures reported by field studies[7,16]. Eoarchean structures show intense deformation and are sometimes interpreted as subduction–accretion terranes[37] or the result of hot orogens[38]. The only known cratons from this period have been found in the Itsaq gneiss complex in west Greenland and in the Superior Province in Canada[7]. Palaeoarchean felsic material can be found in the Kaapvaal craton (mainly in South Africa) and in the Pilbara craton (Western Australia). In both of these locations, the crust has seemingly experienced an internal overturn, forming TTG domes surrounded by komatiitic and basaltic 'keels' filled with sediments. The appearance of these dome and keel geometries is thought to be possible only because of the formation of a very viscous sub-continental lithospheric mantle, strong enough to hold the felsic crust in place despite its diapirism[39]. Additionally, it appears that the felsic plutonism generating the dome and keel structures is linked to several pulses of magmatism thought to be due to a stationary plume below the craton[40]. Thus, field geologists report two main types of Archean material: Eoarchean stacked terranes showing very intense deformation and Paleoearchean dome and keel structures apparently requiring more moderate convection.

The apparently quiescent phase of the Palaeoarchean period seems to end at the start of the Mesoarchean (3.2 billion years ago), at which point more deformation is observed. This has been interpreted as the onset of plate tectonics[7], but this question is beyond the scope of the present Letter and we will only note here that important deformation is reported to start at 3.2 billion years ago.

Our numerical simulations are in good agreement with the main result of these field observations. Extended Data Fig. 1 represents a comparison of our simulations (bottom panel) with the field data previously mentioned (top panel) throughout time. In agreement with the milonitized stacked terranes from the Eoarchean in west Greenland and the Superior Province, we always observe an initial phase of intense deformation in our simulations. This vigorous period can be seen in Fig. 2a (left, the 'dripping' phase) and lasts for one hundred million years to up to seven hundred million years depending on the rheology of the lithosphere (see red and brownish regions at the bottom of Extended Data Fig. 1). The dripping phase occurs as a result of the following model assumptions: the very high initial core temperature[41] produces intense plumes and the upper mantle is fully enriched. A large amount of mafic crust is produced during these hundreds of millions of years. Following this, we observe both dripping of eclogitic chunks hundreds of kilometres in size and proto-subduction-like surface tectonics, as can be seen in Fig. 2. Such behaviour suggests that Eoarchean geodynamics might have been a combination of vertical tectonomagmatic processes and short-lived plate-tectonic-like events that would be difficult to interpret applying only one paradigm. Most of the low- and medium-pressure TTG rocks are formed during this period of time.

The dripping phase is always followed by a 'stagnant lid' period which would offer the stability required for the formation of the dome and keel structures (yellow regions in the bottom panel of Extended Data Fig. 1). Moreover, we do observe a surprising spatial stability of the plumes, due to the settlement and slow warming of the enormous eclogitic blocks at the core–mantle boundary. Mainly high-pressure TTGs are formed during this phase although a small amount of medium-pressure TTGs are also produced. It can be expected here that regional crustal overturn events would cause the formation of more medium- and low-pressure TTG rocks.

Interestingly, very intense resurfacing events (purple regions in Extended Data Fig. 1) sometimes follow the quiescent phase, recycling most of the mafic crust still present. Extended Data Fig. 1 shows that major resurfacing events occur after 800 million years of Earth's evolution (that is, at exactly 3.2 billion years ago) for an intrusion efficiency of 90%. Yet this secondary resurfacing episode due to the re-activation of global convection (once the eclogite blocks at the core–mantle boundary are warm enough) can happen at various times of Earth's evolution. Overall, the simulations with an intrusion efficiency of 90% generate geodynamical transitions consistent with the general geological record and produce the expected amounts of TTG rocks.

In summary, we show that our simulations not only confirm the importance of intrusive magmatism for the production of proto-continental crust, they are also in agreement with geological observations for Archean cratons. However, further model improvements are required (and in progress) for a more detailed comparison of our models with field data. We expect that few of the low- and medium-pressure TTGs produced during the dripping phase would be preserved (which we cannot yet see in our models) and more of these TTGs could be produced during the dome and keel process in the quiescent phase. We have shown that the initial dripping phase generates a mix of vertical and short-lived horizontal tectonics for some hundreds of millions of years. The blocks of mafic material produced during this initial episode and sinking to the core–mantle boundary might be responsible for a stagnant phase a few hundreds of millions of years long. And finally, a more global convection phase can be expected when the eclogite at the core–mantle boundary is warm enough. Overall, these qualitative observations are in good agreement with quantitative measurements of volumes of TTG rocks produced when (and only when) a high intrusion efficiency is considered.

Implications of the present study for the dynamics of Venus. It has been suggested recently that Venus—although lacking continental crust—might be a better analogue for the Archean Earth than Jupiter's moon Io[7,42,43]. For this purpose we compile briefly the current knowledge on Venus tectonics and compare it with results of numerical models, as follows. The small number of craters on Venus led to the conclusion that the planet experienced a global resurfacing event in the past billion years[21,42,44–46]. Venus-like global resurfacing events can be observed in global models taking both extrusive[22] and intrusive crust formation models[47] (see also Fig. 2), so additional geological constraints are necessary to distinguish between crust-formation scenarios. Spectrometric measurements at the Venera and Vega landing sites showed that the surface of Venus is dominated by basaltic material[48], so a certain fraction of the generated melt must be extruded on Venus. However, there are also clear signs of lithosphere deformation, such as novae[49,50], coronae[51–54] and tessera terrains[55], whereas the existence of subduction zones remains uncertain[56]. Dike intrusions have been suggested to be important for the formation of novae[57] and structural analysis indicates that novae can evolve into coronae-like structures over time[50]. Corona-formation models involving flexure of a thick and strong lithosphere[58,59] reproduced part of the nine observed topographic groups of coronae; however, these models tend to overestimate the size of coronae. The model of a thick and cold lithosphere has been challenged by recent studies suggesting a low elastic thickness of less than 20 km for large parts of Venus (which implies a thin and warm Venus lithosphere[60,61]). A recent study taking these new data into account by modelling melt intrusion into the lower crust of Venus showed that coronae can evolve self-consistently from novae structures[62], in agreement with geological data. In conclusion, a crust formation model incorporating both extrusive and intrusive crust formation seems to be necessary to explain the observed tectonics on present-day Venus.

Data availability. The data that support the findings of this study are available from the corresponding author upon reasonable request. Source Data for Figs 2 and 3 are available in the online version of the paper.

23. Tackley, P. J. Modelling compressible mantle convection with large viscosity contrasts in a three-dimensional spherical shell using the yin-yang grid. *Phys. Earth Planet. Inter.* **171,** 7–18 (2008).
24. Hernlund, J. W. & Tackley, P. J. Modeling mantle convection in the spherical annulus. *Phys. Earth Planet. Inter.* **171,** 48–54 (2008).
25. Amestoy, P., Duff, I. & l'Excellent, J.-Y. Multifrontal parallel distributed symmetric and unsymmetric solvers. *Comput. Methods Appl. Mech. Eng.* **184,** 501–520 (2000).
26. Harlow, F. & Welch, J. Numerical calculation of time-dependent viscous incompressible flow of fluid with a free surface. *Phys. Fluids* **8,** 2182 (1965).
27. Nakagawa, T. & Tackley, P. Thermo-chemical structure in the mantle arising from a three-component convective system and implications for geochemistry. *Phys. Earth Planet. Inter.* **146,** 125–138 (2004).
28. Nakagawa, T. & Tackley, P. Influence of magmatism on mantle cooling, surface heat flow and Urey ratio. *Earth Planet. Sci. Lett.* **329/330,** 1–10 (2012).
29. Karato, S.-I. & Wu, P. Rheology of the upper mantle: a synthesis. *Science* **260,** 771–778 (1993).
30. Yamazaki, D. & Karato, S.-I. Some mineral physics constraints on the rheology and geothermal structure of Earth's lower mantle. *Am. Mineral.* **86,** 385–391 (2001).
31. Tackley, P., Ammann, M., Brodholt, J., Dobson, D. & Valencia, D. Mantle dynamics in super-Earths: post-perovskite rheology and self-regulation of viscosity. *Icarus* **225,** 50–61 (2013).
32. Čížková, H., van den Berg, A., Spakman, W. & Matyska, C. The viscosity of Earth's lower mantle inferred from sinking speed of subducted lithosphere. *Phys. Earth Planet. Inter.* **200/201,** 56–62 (2012).
33. Irifune, T. & Ringwood, A. Phase transformations in subducted oceanic crust and buoyancy relationships at depths of 600-800 km in the mantle. *Earth Planet. Sci. Lett.* **117,** 101–110 (1993).
34. Ono, S., Ito, E. & Katsura, T. Mineralogy of subducted basaltic crust (MORB) from 25 to 37 GPa, and chemical heterogeneity of the lower mantle. *Earth Planet. Sci. Lett.* **190,** 57–63 (2001).
35. Moyen, J.-F. & Stevens, G. in *Archean Geodynamics and Environments* (eds Benn, K., Mareschal, J.-C. & Condie, K.) 149–178 (AGU, 2006).
36. Van Kranendonk, M. in *Earth's Oldest Rocks* (eds Kranendonk, M. V., Smithies, R. & Bennet, V.) 1st edn, *Developments in Precambrian Geology* Vol. 15, 1105–1116 (Elsevier, 2007).
37. Nutman, A. *et al.* in *Earth Accretionary Systems in Space and Time* (eds Cawood, P. & Kröner, A.) 1st edn, Vol. 318, 127–154 (Spec. Publ. Geol. Soc. Lond., GSL, 2009).
38. van Hunen, J. & Moyen, J.-F. Archean subduction: fact or fiction? *Annu. Rev. Earth Planet. Sci.* **40,** 195–219 (2012).
39. Griffin, W. & O'Reilly, S. in *Earth's Oldest Rocks* (eds Kranendonk, M. V., Smithies, R. & Bennet, V.) 1st edn, *Developments in Precambrian Geology* Vol. 15, Ch. 8.2, 1013–1035 (Elsevier, 2007).
40. Hickman, A. & Kranendonk, M. V. in *The Precambrian Earth: Tempos and Events* Vol. 12, 118–139 (Elsevier, 2004).
41. Labrosse, S., Hernlund, J. & Hirose, K. in *The Early Earth* 123–142 (John Wiley & Sons, 2015).
42. Harris, L. & Bédard, J. in *Evolution of Archean Crust and Early Life* (eds Dilek, Y. & Furnes, H.) *Modern Approaches In Solid Earth Sciences* Vol. 7, Ch. 9, 215–288 (Springer, 2014).
43. Harris, L. & Bédard, J. in *Volcanism and Tectonism Across the Inner Solar System* (eds Platz, T., Massironi, M., Byrne, P. K. & Hiesinger, H.) Vol. 401, 327–356 (Spec. Publ. Geol. Soc. Lond., GSL, 2015).
44. Schaber, G. *et al.* Geology and distribution of impact craters on Venus: what are they telling us? *J. Geophys. Res.* **97,** 13257–13301 (1992).
45. Herrick, R. Resurfacing history of Venus. *Geology* **22,** 703–706 (1994).
46. McKinnon, W., Zahnle, K., Ivanov, B. & Melosh, H. in *Venus II* (eds Bougher, S., Hunten, D. & Phillips, R.) 969–1014 (Univ. Arizona Press, 1997).
47. Tackley, P. in *European Geosciences Union General Assembly Conference Abstracts* Vol. 17, 13804 (EGU, 2015).
48. Basilevsky, A. & Head, J. The surface of Venus. *Rep. Prog. Phys.* **66,** 1699–1734 (2003).
49. Aittola, M. & Kostama, V.-P. Venusian novae and arachnoids: characteristics, differences and the effect of the geological environment. *Planet. Space Sci.* **48,** 1479–1489 (2000).
50. Krassilnikov, A. & Head, J. Novae on Venus: geology, classification, and evolution. *J. Geophys. Res.* **108,** 5108 (2003).
51. Barsukov, V. *et al.* Preliminary evidence on the geology of Venus from radar measurements by the Venera 15 and 16 probes. *Geokhimia* **12,** 1811–1820 (1984).
52. Stofan, E. *et al.* Global distribution and characteristics of coronae and related features on Venus: implications for origin and relation to mantle processes. *J. Geophys. Res.* **97,** 13347–13378 (1992).
53. Stofan, E., Smrekar, S., Tapper, S., Guest, J. & Grindrod, P. Preliminary analysis of an expanded corona database for Venus. *Geophys. Res. Lett.* **28,** 4267–4270 (2001).
54. Grinrod, P. & Hoogenboom, T. Venus: the corona conundrum. *Astron. Geophys.* **47,** 16–21 (2006).
55. Bindschadler, D. & Head, J. Tessera terrain, Venus: characterization and models for origin and evolution. *J. Geophys. Res.* **96,** 5889–5907 (1991).
56. Sandwell, D. & Schubert, G. Evidence for retrograte lithosphere subduction on Venus. *Science* **257,** 766–770 (1992).
57. Ernst, R., Grosfils, E. & Mége, D. Giant dike swarms: Earth, Venus, and Mars. *Annu. Rev. Earth Planet. Sci.* **29,** 489–534 (2001).
58. Smrekar, S. & Stofan, E. Corona formation and heat loss on Venus by coupled upwelling and delamination. *Science* **277,** 1289–1294 (1997).
59. Hoogenboom, T. & Houseman, G. Rayleigh-Taylor instability as a mechanism for corona formation on Venus. *Icarus* **180,** 292–307 (2006).
60. Anderson, F. & Smrekar, S. Global mapping of crustal and lithospheric thickness on Venus. *J. Geophys. Res.* **111,** E08006 (2006).
61. James, P., Zuber, M. & Phillips, R. Crustal thickness and support of topography on Venus. *J. Geophys. Res.* **118,** 859–875 (2013).
62. Gerya, T. Plume-induced crustal convection: 3D thermomechanical model and implications for the origin of novae and coronae on Venus. *Earth Planet. Sci. Lett.* **391,** 183–192 (2014).
63. Nutman, A. P. Antiquity of the oceans and continents. *Elements* **2,** 4 (2006).

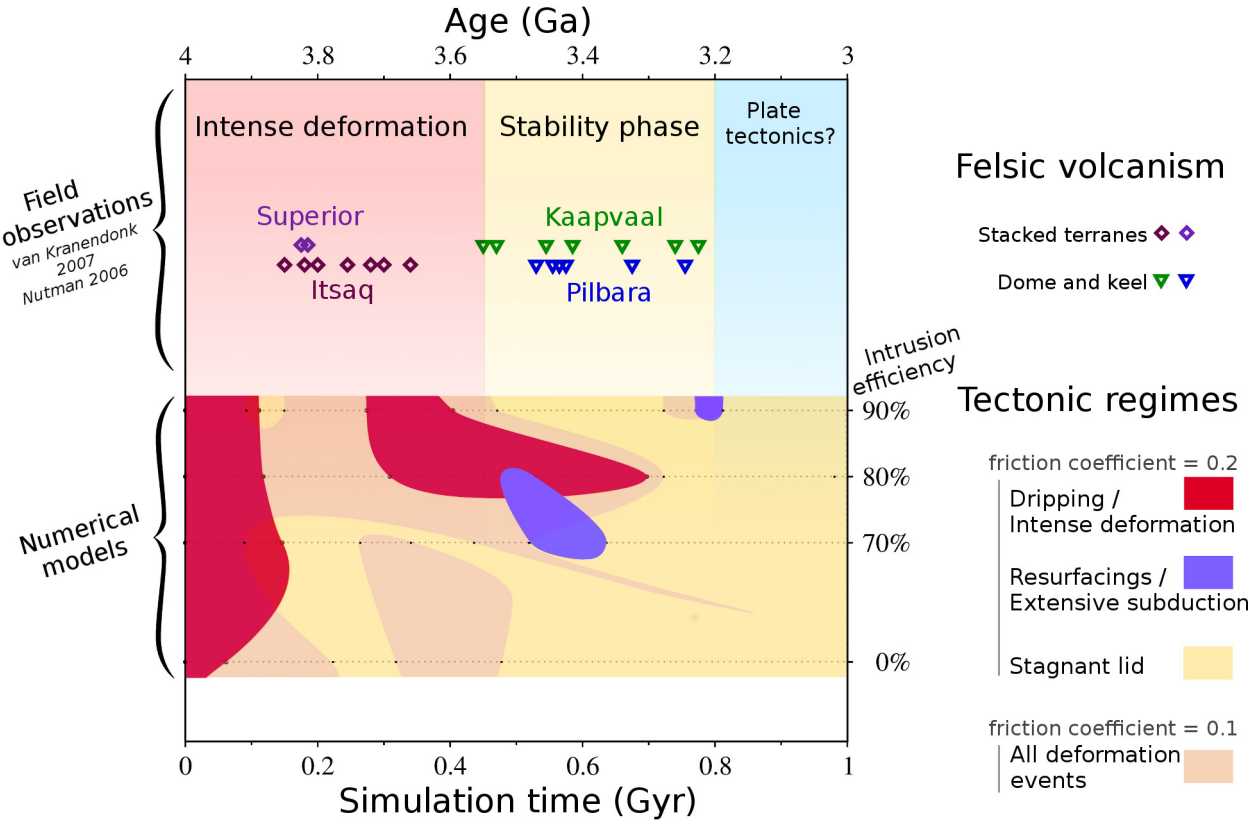

Extended Data Figure 1 | Comparison of field data (and their geodynamic interpretation) and the tectonic regimes self-consistently obtained in our simulations (see Methods). Numerical models always show some intense deformation during the first hundreds of millions of years and then reach a stagnant phase. Massive resurfacing events (purple areas) are sometimes observed after a long stability period, consistent with field data[36,63] interpretations. Ga, billions of years ago.

Extended Data Table 1 | Required *P* (GPa) and *T* (°C) conditions for TTG formation

Low and medium pressure TTG		
$760 - 60\,(P-1)^2$	$< T <$	$1000 - 150\left(\frac{P-1.2}{1.2}\right)^2$
$-0.5\left(\frac{T-870}{220}\right)$	$< P <$	$1.5 + 0.7\left(\frac{T-700}{200}\right)$
High pressure TTG		
1000	$< T <$	$1100 + 50\left(\frac{P-3.5}{3.5}\right)^2$
$2.35 + 0.15\left(\frac{T-1000}{100}\right)$	$< P <$	5

Low-pressure TTGs form at $P < 1$ GPa, while medium-pressure TTGs require higher pressures. Pressure–temperature windows are taken from figure 12 of ref. 11. TTG formation occurs only when both basalt and water contents are greater or equal to 50% of the imposed surface hydration conditions.

Extended Data Table 2 | Final global volumes (in cubic kilometres, after a billion years) for all simulations

Setup		TTG Volumes (km^3)				Relative percentages		
f.	I. (%)	Low P.	Med. P.	High P.	All	Low P.	Med. P.	High P.
0.1	0	$2.45 \cdot 10^7$	$4.89 \cdot 10^6$	$5.35 \cdot 10^7$	$8.29 \cdot 10^7$	29.5	5.9	64.6
0.1	20	$9.93 \cdot 10^7$	$1.87 \cdot 10^8$	$5.29 \cdot 10^7$	$3.39 \cdot 10^8$	29.3	55.1	15.6
0.1	40	$1.79 \cdot 10^8$	$3.67 \cdot 10^8$	$9.22 \cdot 10^7$	$6.39 \cdot 10^8$	28.0	57.5	14.4
0.1	60	$3.44 \cdot 10^8$	$2.2 \cdot 10^8$	$5.25 \cdot 10^7$	$6.16 \cdot 10^8$	55.7	35.8	8.5
0.1	70	$3.04 \cdot 10^8$	$1.7 \cdot 10^8$	$3.42 \cdot 10^7$	$5.09 \cdot 10^8$	59.8	33.5	6.7
0.1	80	$3.06 \cdot 10^8$	$1.89 \cdot 10^8$	$2.04 \cdot 10^7$	$5.15 \cdot 10^8$	59.4	36.6	4.0
0.1	90	$4.09 \cdot 10^8$	$1.76 \cdot 10^8$	$2.34 \cdot 10^7$	$6.09 \cdot 10^8$	67.2	28.9	3.8
0.2	0	$5.98 \cdot 10^6$	$3.96 \cdot 10^6$	$4.02 \cdot 10^8$	$4.12 \cdot 10^8$	1.5	1.0	97.6
0.2	20	$4.02 \cdot 10^7$	$1.21 \cdot 10^8$	$3.1 \cdot 10^8$	$4.72 \cdot 10^8$	8.5	25.7	65.7
0.2	40	$9.24 \cdot 10^7$	$6.35 \cdot 10^8$	$8.59 \cdot 10^8$	$1.59 \cdot 10^9$	5.8	40.0	54.2
0.2	60	$2.16 \cdot 10^8$	$6.98 \cdot 10^8$	$6.01 \cdot 10^8$	$1.52 \cdot 10^9$	14.2	46.1	39.7
0.2	70	$4.7 \cdot 10^8$	$6.41 \cdot 10^8$	$2.84 \cdot 10^8$	$1.4 \cdot 10^9$	33.7	45.9	20.4
0.2	80	$4.84 \cdot 10^8$	$4 \cdot 10^8$	$1.41 \cdot 10^8$	$1.02 \cdot 10^9$	47.2	39.0	13.8
0.2	90	$4.26 \cdot 10^8$	$3.08 \cdot 10^8$	$1.22 \cdot 10^8$	$8.55 \cdot 10^8$	49.8	36.0	14.2
0.3	0	$2.55 \cdot 10^6$	$2.39 \cdot 10^6$	$4.8 \cdot 10^8$	$4.85 \cdot 10^8$	0.5	0.5	99.0
0.3	20	$1.51 \cdot 10^7$	$4.72 \cdot 10^7$	$5.39 \cdot 10^8$	$6.01 \cdot 10^8$	2.5	7.9	89.6
0.3	40	$2.72 \cdot 10^7$	$2.42 \cdot 10^8$	$8.01 \cdot 10^8$	$1.07 \cdot 10^9$	2.5	22.6	74.9
0.3	60	$1.61 \cdot 10^8$	$8.33 \cdot 10^8$	$6.33 \cdot 10^8$	$1.63 \cdot 10^9$	9.9	51.2	38.9
0.3	70	$2.02 \cdot 10^8$	$3.44 \cdot 10^8$	$5.95 \cdot 10^8$	$1.14 \cdot 10^9$	17.7	30.1	52.1
0.3	80	$4.23 \cdot 10^8$	$3.91 \cdot 10^8$	$2.89 \cdot 10^8$	$1.1 \cdot 10^9$	38.3	35.5	26.2
0.3	90	$2.03 \cdot 10^8$	$1.75 \cdot 10^8$	$5.04 \cdot 10^7$	$4.29 \cdot 10^8$	47.4	40.8	11.8
0.4	0	$5 \cdot 10^5$	$6.2 \cdot 10^6$	$3.83 \cdot 10^8$	$3.9 \cdot 10^8$	0.1	1.6	98.3
0.4	20	$3.9 \cdot 10^6$	$3.19 \cdot 10^7$	$3.43 \cdot 10^8$	$3.79 \cdot 10^8$	1.0	8.4	90.5
0.4	40	$1.89 \cdot 10^7$	$2.94 \cdot 10^8$	$8.68 \cdot 10^8$	$1.18 \cdot 10^9$	1.6	24.9	73.5
0.4	60	$8.24 \cdot 10^7$	$4.19 \cdot 10^8$	$7.45 \cdot 10^8$	$1.25 \cdot 10^9$	6.6	33.6	59.8
0.4	70	$1.4 \cdot 10^8$	$4.37 \cdot 10^8$	$5.84 \cdot 10^8$	$1.16 \cdot 10^9$	12.1	37.6	50.3
0.4	80	$2.34 \cdot 10^8$	$3.59 \cdot 10^8$	$3.44 \cdot 10^8$	$9.37 \cdot 10^8$	25.0	38.3	36.7
0.4	90	$1.99 \cdot 10^8$	$2.24 \cdot 10^8$	$4.15 \cdot 10^7$	$4.65 \cdot 10^8$	42.9	48.2	8.9
0.5	0	$6.31 \cdot 10^5$	$5.72 \cdot 10^6$	$4.4 \cdot 10^8$	$4.47 \cdot 10^8$	0.1	1.3	98.6
0.5	20	$2.39 \cdot 10^6$	$2.36 \cdot 10^7$	$4.58 \cdot 10^8$	$4.84 \cdot 10^8$	0.5	4.9	94.6
0.5	40	$2.03 \cdot 10^7$	$2.48 \cdot 10^8$	$9.1 \cdot 10^8$	$1.18 \cdot 10^9$	1.7	21.0	77.3
0.5	60	$3.52 \cdot 10^7$	$3.72 \cdot 10^8$	$7.56 \cdot 10^8$	$1.16 \cdot 10^9$	3.0	32.0	65.0
0.5	70	$1.06 \cdot 10^8$	$3.72 \cdot 10^8$	$6.57 \cdot 10^8$	$1.13 \cdot 10^9$	9.4	32.8	57.8
0.5	80	$1.86 \cdot 10^8$	$3.43 \cdot 10^8$	$3.91 \cdot 10^8$	$9.2 \cdot 10^8$	20.2	37.3	42.5
0.5	90	$1.69 \cdot 10^8$	$1.77 \cdot 10^8$	$5.08 \cdot 10^7$	$3.97 \cdot 10^8$	42.7	44.5	12.8
0.6	0	$1.32 \cdot 10^6$	$1.38 \cdot 10^7$	$2.91 \cdot 10^8$	$3.06 \cdot 10^8$	0.4	4.5	95.1
0.6	20	$1.96 \cdot 10^6$	$2.86 \cdot 10^7$	$4.4 \cdot 10^8$	$4.71 \cdot 10^8$	0.4	6.1	93.5
0.6	40	$1.91 \cdot 10^7$	$2.57 \cdot 10^8$	$8.66 \cdot 10^8$	$1.14 \cdot 10^9$	1.7	22.5	75.8
0.6	60	$6.26 \cdot 10^7$	$4.58 \cdot 10^8$	$8.01 \cdot 10^8$	$1.32 \cdot 10^9$	4.7	34.7	60.6
0.6	70	$9.72 \cdot 10^7$	$4.87 \cdot 10^8$	$6.34 \cdot 10^8$	$1.22 \cdot 10^9$	8.0	40.0	52.0
0.6	80	$1.49 \cdot 10^8$	$3.25 \cdot 10^8$	$3.66 \cdot 10^8$	$8.41 \cdot 10^8$	17.8	38.7	43.6
0.6	90	$1.43 \cdot 10^8$	$1.29 \cdot 10^8$	$1.38 \cdot 10^7$	$2.86 \cdot 10^8$	50.1	45.1	4.8

"f." is the friction coefficient and "I." is the intrusion efficiency.

Extended Data Table 3 | Rheological properties in the viscous regime

Property	Symbol	Value	Units
- Upper Mantle			
Activation Energy	E_1	300	kJ/mol
Activation Volume	V_1	5.00	cm^3/mol
Viscosity Multiplier	$\Delta\eta_1$	1.0	
- Lower Mantle			
Activation Energy	E_2	370	kJ/mol
Activation Volume	V_2	3.65	cm^3/mol
Pressure scale	P_2	200	GPa
Viscosity Multiplier	$\Delta\eta_2$	30	
- Post-perovskite layer			
Activation Energy	E_3	162	kJ/mol
Activation Volume	V_3	1.40	cm^3/mol
Pressure scale	P_3	1610	GPa
Viscosity Multiplier	$\Delta\eta_3$	0.1	

Extended Data Table 4 | Phase-change parameters for olivine and pyroxene-garnet phase systems

Depth (km)	Temperature (K)	$\Delta\rho$ (kg/m^3)	γ (MPa/K)
Olivine			
$\rho_s = 3240$ kg/m^3			
410	1600	180	2.5
660	1900	400	-2.5
2740	2300	61.6	10
Pyroxene-Garnet			
$\rho_s = 3080$ kg/m^3			
60	1000	350	0
400	1600	150	1
720	1900	400	1
2740	2300	61.6	10

ρ_s is the surface density, $\Delta\rho$ is the density jump across a phase transition and γ is the Clapeyron slope.